Crystal structure and high temperature X-ray diffraction study of thermoelectric chimney-ladder FeGeγ ($\gamma \approx 1.52$)

S. Le Tonquesse, C. Hassam, Y. Michiue, Yoshitaka Matsushita, Mathieu Pasturel, T. Mori, Tohru Suzuki, David Berthebaud

Crystal structure and high temperature X-ray diffraction study of thermoelectric chimney-ladder $FeGe_\gamma$ ($\gamma \approx 1.52$)

Sylvain Le Tonquesse[a,c], Christopher Hassam[a,b], Yuichi Michiue[d], Yoshitaka Matsushita[c], Mathieu Pasturel[e], Takao Mori[d], Tohru S. Suzuki[c], David Berthebaud[a,]

[a]*CNRS-Saint Gobain-NIMS, UMI 3629, Laboratory for Innovative Key Materials and Structures (LINK), National Institute for Materials Science, Tsukuba 305-0044, Japan*
[b]*Laboratoire CRISMAT, UMR 6508, CNRS, ENSICAEN, 6 Boulevard du Maréchal Juin, 14050 Caen Cedex 04, France*
[c]*National Institute for Materials Science, 1-2-1 Sengen, Tsukuba, Ibaraki, 305-0047, Japan*
[d]*National Institute for Materials Science (NIMS), MANA, 1-1-1 Namiki, Tsukuba 305-0044, Japan*
[e]*Univ Rennes, CNRS, Institut des Sciences Chimiques de Rennes - UMR6226, 35042 Rennes, France*

Abstract

The crystal structure of Nowotny chimney-ladder phase $FeGe_\gamma$ with $\gamma \approx 1.52$ was studied by X-ray diffractometry from 300 K to 850 K. The diffraction patterns were fitted by Rietveld refinement considering an incommensurate composite crystal structure. The refined crystal structure of $FeGe_\gamma$ is described in details and compared to $MnSi_\gamma$, a thermoelectric material with $\gamma \approx 1.74$. The lattice parameters a, c_{Fe} and c_{Ge} were found to increase with the temperature following a polynomial law, while the modulation vector component γ remained constant up to the peritectoid decomposition into FeGe and $FeGe_2$. Within the temperature range considered, the linear and volumetric thermal expansion parameters increased from about 3×10^{-6} K^{-1} to 10×10^{-6} K^{-1} and from 9.6×10^{-6} K^{-1} to 31.5×10^{-6} K^{-1}, respectively.

Keywords:
X-ray diffraction, Intermetallics, Thermoelectic materials, Crystal structure, Thermal expansion

*David.BERTHEBAUD@cnrs.fr

1. Introduction

Heat losses are omnipresent in modern societies. In combustion engines heat losses occur through the exhaust, in electronics there are heat losses due to Joule heating, even the human body experiences heat loss due to thermoregulation. The direct conversion of thermal energy from these heat losses into electricity by an all-solid-state thermoelectric (TE) generator is a promising way to supply power to the ever more numerous and autonomous sensors and microelectronic devices pervading society [1, 2, 3]. The most common design of generator is an assembly of *n*- and *p*-type TE materials connected electrically in series and thermally in parallel between two electrically insulating and thermally conducting ceramic plates [4, 5]. The conversion efficiency of the TE materials is directly related to the adimensional figure of merit ZT, which is defined at a given temperature T (K) as:

$$ZT = \frac{\alpha^2 T}{\rho \kappa} \tag{1}$$

where α (V K^{-1}) is the Seebeck coefficient, ρ (Ω m) the electrical resistivity and κ (W m^{-1} K^{-1}) the thermal conductivity.

The Nowotny chimney-ladder compound MnSi$_\gamma$ with $\gamma \approx 1.74$ often refereed to as higher manganese silicide (HMS), is a highly promising *p*-type TE material because it is composed of inexpensive and non-toxic elements [6, 7]. Its incommensurate composite crystal structure [8] results in a relatively low thermal conductivity of about 2.5 W m^{-1} K^{-1} and ZT of 0.4 at 800 K [9, 10]. However, the large scale development of mid-temperature TE generators (600 - 800 K) based on this material remains limited due to the lack of an *n*-type counterpart with comparable thermoelectric and mechanical properties [11]. Among the other silicides, the current best options are *n*-type Co-doped FeSi$_2$ whose ZT only reaches about 0.2 in the same conditions [12] or Sn-doped Mg$_2$Si which

has much lower mechanical and chemical resistance properties [13].

In 2000, a new Nowotny chimney-ladder Fe-Ge compound with a composition close to Fe_2Ge_3 was discovered by Gerasimov *et al.* [14]. The late discovery of this compound is explained by its slow peritectoid formation below 850 K from the kinetically stable FeGe and $FeGe_2$. Later, Li *et al.* demonstrated by electron diffraction that it crystallizes in an incommensurate composite structure with modulation wave vector $\boldsymbol{q} = \gamma \boldsymbol{c}^*$, which is isostructural to HMS [15]. The crystal structure is composed of two interpenetrating [Fe] and [Ge] tetragonal subsystems with common a but different and incommensurate c_{Fe} and c_{Ge} lattice parameters (see Figure 1). As both subsystems have 4 atoms per unit cell, the modulation wave vector component, $\gamma = c_{Fe}/c_{Ge}$, dictates the stoichiometry of the compound. For this reason, the phase is better described by the chemical formula $FeGe_\gamma$ with γ close but not exactly equal to 1.52. The TE properties of $FeGe_\gamma$ were first reported for a bulk polycrystalline sample by Sato *et al.* who established an n-type conductivity and a high ZT of approximately 0.6 at 700 K [16]. As for HMS, the low thermal conductivity of 2.5 W m^{-1} K^{-1} at 700 K is attributed to the complex crystal structure which efficiently scatters heat-carrying phonons. This material has garnered much interest in recent years and is now considered as a promising high-performance n-type counterpart to HMS. Verchenko *et al.* first managed to grow $FeGe_\gamma$ single crystal by a chemical transport method [17]. Surprisingly, single crystal X-ray diffraction (XRD) data indicates a commensurate structure Fe_2Ge_3 isostructural to Ru_2Sn_3 with space group $P\bar{4}c2$ (no. 116) and lattice parameters of $a = 5.5848(8)$ Å and $c = 8.9400(18)$ Å. However, this structural model was not supported by powder XRD and electron diffraction patterns which clearly indicate incommensurability. Despite these divergent results, no detailed structural analysis of polycrystalline $FeGe_\gamma$ has been reported. A better description of the $FeGe_\gamma$ structure is of the highest importance to gain a better understanding of the structure-property relationships in Nowotny chimney-ladder compounds.

In this article, the crystal structure of polycrystalline $FeGe_\gamma$ is studied by powder XRD and refined by the Rietveld method considering a composite crystal model in (3+1) dimension. The discussion is focused on the structure and microstructure of $FeGe_\gamma$ in comparison with the better-known $MnSi_\gamma$. The thermal behavior of the structure is also investigated up to the decomposition temperature around 850 K. The evolution of the lattice parameters at high temperatures and the thermal expansion coefficients are determined and discussed as they are of practical importance for TE generator design and manufacturing.

2. Experimental section

For the synthesis of $FeGe_\gamma$, first, elemental powders of Fe ($>$ 99.99 %) and Ge ($>$ 99.99 %) were mixed in a nominal molar ratio of 2:3. 5 g of the powder mixture was then ball-milled in a 400 mL WC vial with Ø=1 cm WC balls for 1 h at 400 rpm under Ar atmosphere. The mixture was then cold pressed and annealed in an evacuated silica tube for 1 month at 773 K.

Powder XRD was realized using a *θ-2θ* Rigaku SmartLab diffractometer equipped with a Cu rotating target, a Ge(111) monochromator set at incident beam side selecting the Cu $K_{\alpha 1}$ radiation (1.54056 Å) and a D/teX Ultra 250 detector. The measurements were performed from 20° to 120° with a step width of 0.020° using variable slits. High temperature measurements were performed at 300 K, 400 K, 500 K, 600 K, 700 K, 800 K and 850 K under dynamic vacuum ($\approx 7\times10^{-3}$ Pa). The X-ray powder patterns were fitted using the JANA2006 software [18]. The peak shapes were modeled using Thompson-Cox-Hastings pseudo-voigt functions [19]. Berar's factors were applied to the estimated standard deviation to obtain more realistic values [20]. The mass fractions of impurities were determined by quantitative Rietveld refinement.

Details about the lattice vectors setting and refinement procedure used in the present work will be discussed briefly here. More general information about

incommensurate crystallography can be found in ref. [21]. In real space, the subsystems [Fe] and [Ge] present conventional 2D periodicity along the *a* and *b* directions but are incommensurate along the *c* direction. The diffraction pattern of $FeGe_\gamma$ is constructed as the superposition of the diffraction patterns of the two incommensurately modulated [Fe] and [Ge] subsystems. Two sets of four reciprocal lattice vectors, M_{Fe} and M_{Ge}, are thus required to fully index the reciprocal lattice of the subsystems. Each set contains three linearly independent basic vectors corresponding to the basic structure and one additional modulation wave vector. Because of the mutual interaction, the modulation of the [Fe] subsystem is determined from the basic reciprocal lattice vectors of the [Ge] subsystem and *vice versa*. Furthermore, the two subsystems share a common reciprocal lattice plane. Only one set of four reciprocal lattice vectors M = ($\boldsymbol{x}_1^*$, $\boldsymbol{x}_2^*$, $\boldsymbol{x}_3^*$, $\boldsymbol{x}_4^*$) is thus required to fully index the composite crystal diffraction patterns. The reciprocal lattice vector sets M_{Fe} and M_{Ge} are defined from the set M by application of the following *W* matrices :

$$W_{Fe} = \begin{pmatrix} 1 & 0 & 0 & 0 \\ 0 & 1 & 0 & 0 \\ 0 & 0 & 1 & 0 \\ 0 & 0 & 0 & 1 \end{pmatrix} \qquad W_{Ge} = \begin{pmatrix} 1 & 0 & 0 & 0 \\ 0 & 1 & 0 & 0 \\ 0 & 0 & 0 & 1 \\ 0 & 0 & 1 & 0 \end{pmatrix} \tag{2}$$

In this setting, the $FeGe_\gamma$ reciprocal lattice parameters are $a^* = \|\boldsymbol{x}_1^*\| = \|\boldsymbol{x}_2^*\|$, $c_{Fe}^* = \|\boldsymbol{x}_3^*\|$, $c_{Ge}^* = \|\boldsymbol{x}_4^*\|$. Since the reciprocal lattice vectors $\boldsymbol{x}_3^*$ and $\boldsymbol{x}_4^*$ are collinear, the modulation vector component γ is equal to $\|\boldsymbol{x}_4^*\| \,/\, \|\boldsymbol{x}_3^*\|$. Four Miller indices *hkl*m are required to index all the Bragg reflections of $FeGe_\gamma$ pattern. In the present settings, the reflections *hk00* are common to both subsystems, *hkl0* corresponds to the [Fe] subsystem main reflections, *hk0m* corresponds to the [Ge] subsystem main reflections and *hklm* (l $\neq$ 0, m $\neq$ 0) are satellite reflections resulting from the modulations of both subsystems. Satellite reflections up to the second order were considered for structural refinements.

The modulation function u(v) describing the displacement of atoms from their average positions in modulated crystals is periodic along the forth superspace direction v [22, 23]. In the case of FeGe$_\gamma$, v is defined for the subsystems [Fe] and [Ge] as:

$$\begin{aligned} v_{Fe} &= t + \gamma \cdot x_3 \\ v_{Ge} &= t + 1/\gamma \cdot x_4 \end{aligned} \tag{3}$$

where t is a constant. The modulation functions can be decomposed using a Fourier series:

$$u(v) = \sum_{k=1}^{k} A^k sin(2\pi k v) + B^k cos(2\pi k v) \tag{4}$$

where the Fourier terms A^k and B^k were refined against the diffraction pattern up to $k = 2$ and $k = 4$ for Fe and Ge modulations, respectively. The following restrains apply to the Fourier terms of the [Ge] subsystem due to superspace symmetry: $A^1_x = A^1_y = B^1_x = -B^1_y$ and $A^3_x = A^3_y = -B^3_x = B^3_y$. Similarly, only the Fourier term B^2_z is allowed by symmetry in the [Fe] subsystem.

Differential scanning calorimetry (DCS) analysis was performed using a Rigaku DSC 8270 apparatus and using Al_2O_3 reference. The analysis was performed from 300 K to 1000 K at a rate of 10 K min^{-1} in a Pt-Rh crucible under N_2 atmosphere.

3. Results and discussion

3.1. Crystal structure of FeGe$_\gamma$ at 300 K

The sample used for diffraction measurement contained 86.1 wt.% of FeGe$_\gamma$ as well as 4.5 wt.% of FeGe ($P2_13$), 5.9 wt.% of $FeGe_2$ ($I4/mcm$) and 3.5 wt.% of

$FeGe_2O_4$ ($Fd\bar{3}m$) as determined by quantitative Rietveld analysis. Single phase sample is very challenging to synthesize because of the slow peritectoid formation of $FeGe_\gamma$ which requires long annealing time. However, the present sample was considered of sufficient quality for XRD analysis as the diffraction peaks of the impurities are well-defined and do not overlap with the phase of interest.

A first attempt to fit the diffraction pattern was made by considering the commensurate Fe_2Ge_3 (or $FeGe_\gamma$ with $\gamma = 1.5$) structure determined by Verchenko *et al.* on single crystalline sample [17]. This structural model (see Table SI. 1) could not, however, satisfactorily fit the data, showing large discrepancies between observed and calculated 2θ positions for many Bragg reflections. As a result, the Rietveld refinement is unstable and high discrepancy values were obtained, *e.g.* $\chi^2 > 100$.

A better agreement with the experimental data was obtained by considering $FeGe_\gamma$ as an incommensurate composite crystal with γ close to but slightly different than 1.5. The (3+1)D space group $I4_1/amd(00\gamma)00ss$ used to describe the structural symmetry [24]. The [Fe] and [Ge] subsystems were generated by placing Fe and Ge atoms in position $x = y = z = 0$ and $x = y = z = 0.25$, respectively. Three lattice parameters, a, c_{Fe} and γ, are refined against the diffraction pattern (see experimental section). The lattice parameter c_{Ge} was deduced from the relation $c_{Fe}/\gamma = c_{Ge}$. Rietveld refined patterns and refined structural parameters can be found in Figure 2 and Table 1, respectively. The fact that only the (3+1)D superspace approach lead to satisfactory agreement with the data is clear evidence of the structural incommensurability of $FeGe_\gamma$. Interestingly, the full width at half maximum of some $hk0m$ ([Ge] subsystem) and $hklm$ (satellite) diffraction peaks are significantly broader than the other reflections. Such anisotropic peak broadening was taken into account in the refinement procedure using the Stephens method [25]. This anisotropic peak broadening is consistent with the high defect concentration evidenced by TEM on the [Ge] subsystem [17]. Similar observations have also been reported in

MnSi$_\gamma$ [26] where the broader *hk*0*m* reflections is also attributed to high density of defects on the ladder [Si] subsystem [27, 10]. However, it should be noted that no peak shape asymmetry is observed for FeGe$_\gamma$, contrarily to HMS [28, 10].

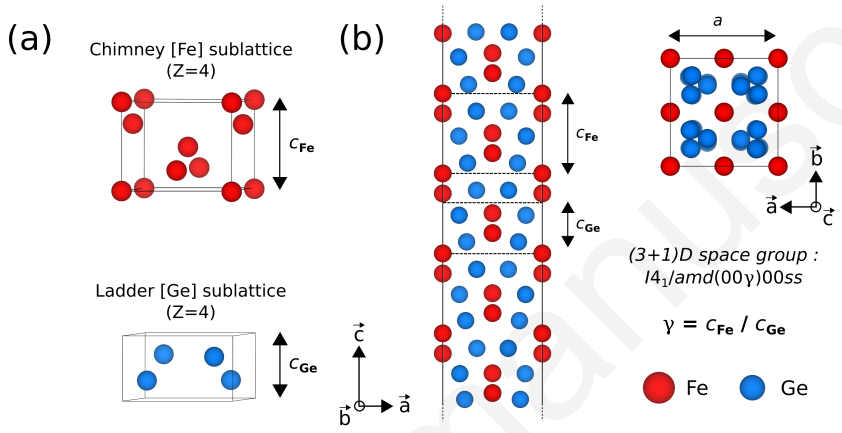

Figure 1: Representations of (a) the structure of the chimney [Fe] and ladder [Ge] subsystems, and (b) the structure of FeGe$_\gamma$ after interpenetration of the two subsystems.

The Rietveld refinement converged to the lattice parameters a = 5.5924(3) Å, c_{Fe} = 4.4948(3) Å and γ = 1.5190(1). Table 1 compares these values to the lattice parameters of isostructural HMS reported by Kikuchi *et al.* [29]. The [Fe] chimney subsystem has a and c parameters 1.2 % and 2.9 % larger, respectively, than the [Mn] subsystem in HMS. This corresponds to a 5.5 % increase of the unit cell volume. The main difference between the two compounds is the 12.6 % smaller γ in FeGe$_\gamma$. As $\gamma = c_{Fe}/c_{Ge}$, it is a direct consequence of the larger c_{Ge} = 2.959(1) Å compared to c_{Si} = 2.5108(1) Å. This causes a 20.7% expansion of the [Ge] ladder unit cell volume that can be explained by the larger atomic radius of Ge (1.25 Å) compared to Si (1.10 Å) [30]. The important volume increase of the ladder unit cell caused by the replacement of Si by Ge manifests predominantly through an expansion of the [Ge] subsystem along the c direction and has only a limited impact on the (a,b)-plane.

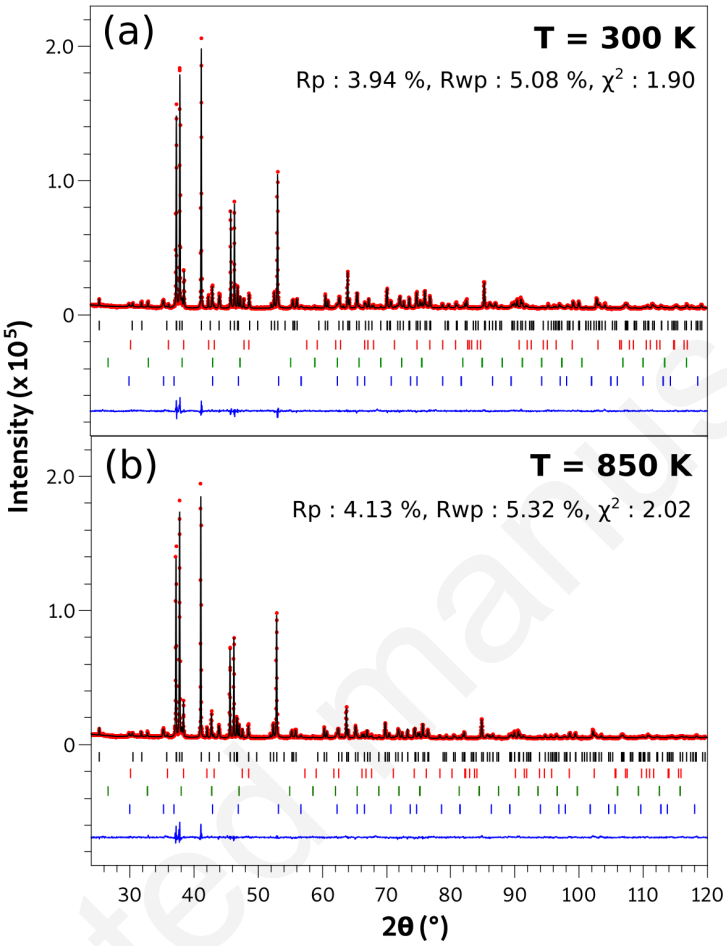

Figure 2: Rietveld refined XRD patterns of $FeGe_\gamma$ measured at 300 K (top) and at 850 K (bottom). The experimental data are plotted in red symbols, the calculated pattern with a black line and the difference with a blue line. The vertical ticks indicate the theoretical Bragg positions of $FeGe_\gamma$ (black), $FeGe_2$ (red), FeGe (green) and Fe_2GeO_4 (blue).

Interaction between the two interpenetrating [Fe] and [Ge] subsystems causes the atoms to be displaced incommensurately from their average positions. All information about the atomic displacements can be fully represented using *t*-plots which consist in plotting the modulation functions $u(v)$ in one superspace unit cell *i.e.* for $0 \leq t \leq 1$. Refined Fourier coefficients are displayed in Table 1 while corresponding $u(v)$ functions are plotted in Figure 3. On the one hand, the displacement of Fe atoms was found to be small along *c* (≤ 0.015 Å)

Table 1: Structural parameters obtained by Rietveld refinement of $FeGe_\gamma$ XRD pattern collected at 300 K. Structural parameters reported in reference [29] for $MnSi_\gamma$ and obtained by powder XRD are also shown for comparison.

	$FeGe_\gamma$	$MnSi_\gamma$
γ	1.5190(1)	1.7387(1)
a (Å)	5.5924(3)	5.5252(1)
Subsystem 1	Fe	Mn
x,y,z	0,0,0	0,0,0
c (Å)	4.4948(3)	4.3656(1)
V (Å^3)	140.57(2)	133.372(3)
B_z^2	-0.003(1)	-0.0147(7)
U_{iso} (Å^2)	0.0296(7)	0.0249(5)
Subsystem 2	Ge	Si
x,y,z	0.25,0.25,0.25	0.25,0.25,0.25
c (Å)	2.959(1)	2.5108(1)
V (Å^3)	92.54(3)	76.652(4)
A_x^1	0.0720(2)	0.0767(3)
A_x^3	-0.0041(3)	0.0092(4)
B_z^4	-0.010(2)	-0.023(2)
U_{iso} (Å^2)	0.0329(6)	0.0245(7)

and null along a and b. On the other hand, Ge has much larger displacement amplitudes, reaching a maximum of about 0.52 Å along a and b. The effect of the Ge modulation in the (a,b)-plane is clearly visible on the c-axis projection of the structure in Figure 1b with the formation of Ge-helices. The displacement amplitude of Ge atoms along the c-axis is much smaller with a maximum of about 0.07 Å. The Fourier coefficients describing the modulation function of [Mn] and [Si] in $MnSi_\gamma$ are also shown for comparison in Table 1 and Figure 3 with dotted lines. The shape of the modulation functions are similar for the two compounds. The only significant difference is the smaller displacements of both Fe and Ge atoms along the c direction (in green in Figure 3).

A direct consequence of the incommensurability is the different coordination environment of all atoms along the c-axis. However, all the possible coordina-

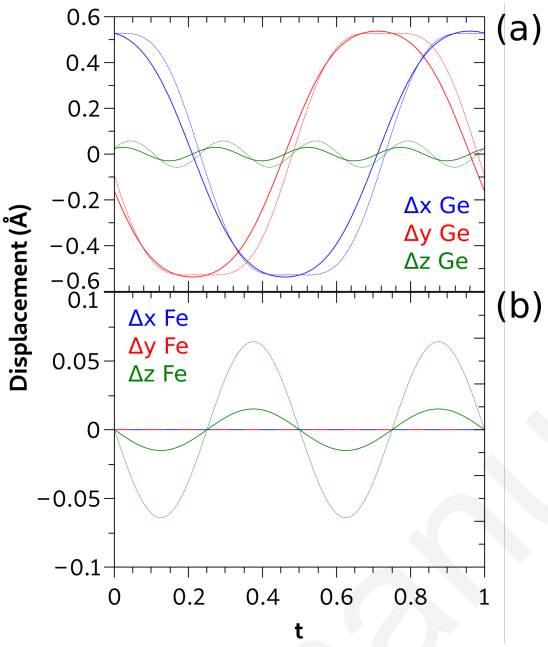

Figure 3: t-plot showing the modulated displacement of Ge (top) and Fe (bottom) atoms around their average positions in $FeGe_\gamma$ (solid lines). The corresponding displacement for Mn and Si in $MnSi_\gamma$ are plotted in dashed lines.

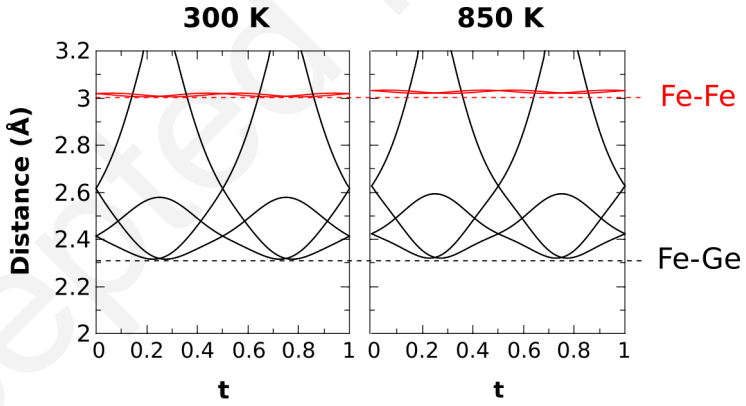

Figure 4: t-plots of the bonds distances around Fe atoms determined from Rietveld refinement at 300 K and 850 K. Fe-Fe bonds are represented in red and Ge-Fe bonds in black.

tion spheres around Fe can be retrieved from the t-plots of the shortest Fe-Fe, Ge-Ge and Fe-Ge bond distances (Figure 4) as well as the Ge-Fe-Ge bond angles. In the present case, it is possible to define every existing coordination

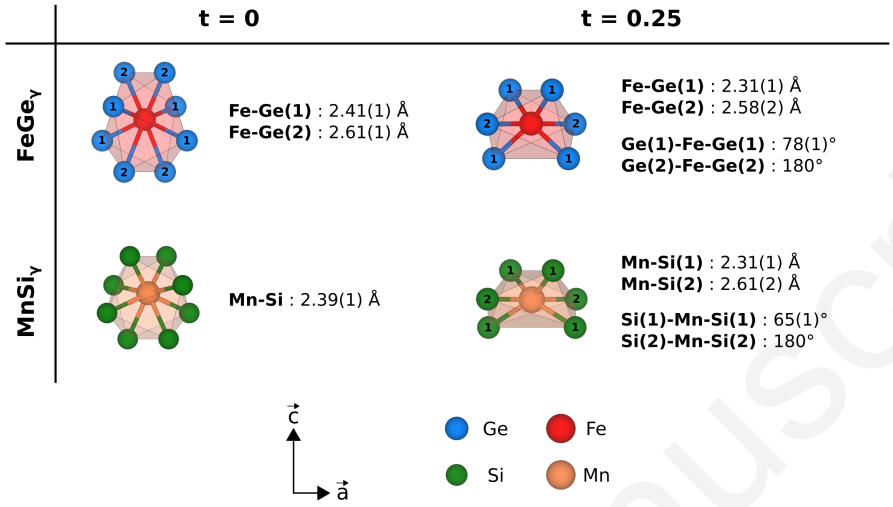

Figure 5: Comparison of the coordination sphere around Fe and Mn atoms in $FeGe_\gamma$ and $MnSi_\gamma$, respectively, at $t = 0$ and $t = 0.25$.

sphere around a given Fe atom as an intermediate case between the two coordination environments found at $t = 0$ and 0.25 (Figure 5). At $t = 0$, Fe is coordinated to 4 Ge at the distance of 2.41(1) Å (labeled Ge(1) in Figure 5) and 4 Ge at 2.61(1) Å (labeled Ge(2)), resulting in a coordination number of 8. The Ge-Fe-Ge bond angles between adjacent Ge atoms are uneven but all have values between 61(1)° and 88(1)°. For $t = 0.25$, the coordination number of Fe is only 6 with 4 Ge at a distance of 2.31(1) Å (labeled Ge(1) in Figure 5) and 2 Ge at 2.58(2) Å(labeled Ge(2)). The smallest Ge(1)-Fe-Ge(1) bond angle is 78(1)° while Ge(2)-Fe-Ge(2) is strictly 180°. It should be noted that the reduction of the coordination number from 8 to 6, when t goes from 0 to 0.25, is compensated by a reduction of the average Fe-Ge bond distance from about 2.5 Å to 2.4 Å. The length of the average Fe-Ge bond distance corresponds well to the closest Fe-Ge distances found in FeGe (2.393, 2.453 and 2.635 Å) [31], $FeGe_2$ (2.546 Å) [32] or $Fe_{1.75}Ge$ (2.343, 2.519 Å) [33]. Figure 5 also shows the corresponding coordination spheres around Mn in HMS determined from the structural parameters reported in Table 1 [29]. The environments of Mn in HMS are very similar to Fe in $FeGe_\gamma$ with the coordination number also going

from 8 to 6 at $t = 0$ and 0.25, respectively. However, two significant differences are : (i) there is a unique Mn-Si distance of 2.39(1) Å at $t = 0$ and (ii) the shortest bond angle Si(1)-Mn-Si(1) at $t = 0.25$ is 65(1)° which is significantly smaller than the respective Ge(1)-Fe-Ge(1) angle of 78(1)°. Both result in a relative elongation of the Fe coordination polyhedra along the c axis compared to $MnSi_\gamma$. These deformations of the Ge polyhedra around Fe is at the origin of the longer c_{Ge} and therefore the lower γ in $FeGe_\gamma$.

3.2. High temperature XRD study of $FeGe_\gamma$

DSC analysis of the sample is presented in Figure SI. 1 and shows a large exothermic peak starting around 850 K upon heating which is attributed to the peritectoid decomposition of $FeGe_\gamma$. XRD confirms that $FeGe_\gamma$ decomposes into FeGe and $FeGe_2$ after the thermal cycling. This result is in full agreement with the accepted Fe-Ge phase diagram [17].

XRD patterns at each measured temperature were fully indexed with the $FeGe_\gamma$ phase and FeGe, $FeGe_2$ and Fe_2GeO_4 impurities. The mass fraction of the impurities remained constant at all temperatures, as expected due to the long annealing (1 month at 773 K) already undergone by the sample. The fitted patterns are represented in Figure 2b and Figure SI. 2,3 and 4 while all the refined parameters are given in Table SI 2. The thermal evolution of the parameters a, c_{Fe}, c_{Ge}, γ, the isotropic atomic displacement parameters U_{iso} for both Fe and Ge and the [Fe] subsystems unit cell volume are plotted in Figure 6 and Figure SI 5. The expansion of lattice parameters are not linear with temperature and are well described using a second order polynomial up to 850 K (Table 2). The a lattice parameter was the most affected with an increase of about 4.5 % from 300 K et 850 K. To a lesser extent, c_{Fe} and c_{Ge} both increased by approximately 3.8 % in the same range. Consequently, the modulation vector γ remained constant over the whole temperature range with an average value of $\gamma = 1.5191 \pm 0.0001$. The atomic displacement parameter of Ge remained larger than for Fe at every temperature. The thermal behaviors of U_{iso} seems to

follow a complex behavior which might be related to some micro-structural effect occurring in the material. Figure 4 shows a comparison of the nearest Fe-Fe and Fe-Ge bond distance t-plots at 300 K and 850 K. The shortest Fe-Fe distance are from 3.006(8) Å to 3.020(8) Å (+ 0.4 %) and the shortest Fe-Ge bond from 2.315(8) to 2.321(7) Å (+ 0.2 %). Except for the small increase of the bond distances, the temperature rise had negligible effect on the modulation and thus on the coordination sphere around Fe atoms.

The stability of γ is an important characteristic that must be taken into account when considering the incorporation of chimney-ladder compounds in thermoelectric generators. For example, in HMS, it was shown both theoretically and experimentally [9] that the valence electron count (VEC) and consequently the concentration of charge carriers (n) is directly linked to the γ value *via* the relation :

$$n = 4 \cdot \frac{14 - VEC}{V_{Mn}} \quad \text{with} \quad VEC = 7 + 4\gamma \tag{5}$$

where V_{Mn} is the volume of the chimney subsystem in HMS. Evolution of γ with the temperature thus has a direct influence on the electrical resistivity and Seebeck coefficient of the material as shown experimentally by Pichon *et al.* [34]. This makes optimization of the thermoelectric legs geometry difficult as well as causing high mechanical stress in the materials. As a similar relation between γ and n is expected in $FeGe_\gamma$, the absence of γ evolution suggests a good stability of the electronic properties within the temperature range of interest.

The thermal expansion is another critical property to take into account when designing mid-temperature thermoelectric generator. Indeed, it is important to match the thermal expansion of the n- and p-type thermoelectric materials as well as with the metallic contacts in order to assure to the device good mechanical resistance upon thermal cycling. The linear α and volumetric β thermal expansion coefficients of $FeGe_\gamma$ given in Table 2 were calculated using the rela-

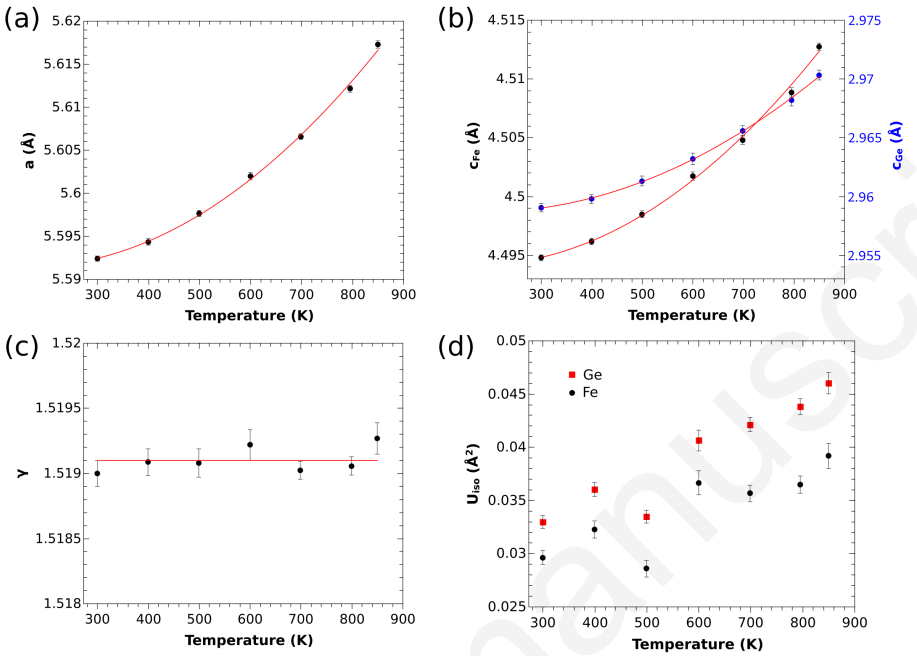

Figure 6: Thermal evolution of the lattice parameters (a) a, (b) c_{Fe} and c_{Ge}, (c) modulation vector coordinate γ and (d) Fe and Ge isotropic atomic displacement parameters U_{iso}.

tions:

$$\alpha_l = \frac{1}{l}\frac{dl}{dT} \qquad \beta = \frac{1}{V_{Fe}}\frac{dV_{Fe}}{dT} \tag{6}$$

where l is a, c_{Fe} or c_{Ge} and V_{Fe} is the volume of the [Fe] subsystem unit cell. Due to the non-linearity of the lattice parameters' respective evolutions with temperature, the thermal expansion coefficients are not constant. At 850 K, the linear expansion coefficients was determined to be approximately 4 times larger than at room temperature and the volumetric thermal expansion coefficient approximately 3 times larger. In the same temperature range, α coefficients of p-type $MnSi_\gamma$ have constant values around 11×10^{-6} K^{-1} [29]. While the thermal expansion coefficient of the two compounds are similar at the targeted application temperature of 800 K, the relatively large difference at lower temperatures may

Table 2: Temperature dependence of the lattice parameters, the linear expansion coefficient α and volumetric expansion coefficient β at 300 K and 850 K.

a (Å)	5.5905(8) - 6.8(3)$\times 10^{-6}$ T + 4.20(3)$\times 10^{-8}$ T^2
c_{Fe} (Å)	4.4935(9) - 4.9(4)$\times 10^{-6}$ T + 3.04(3)$\times 10^{-8}$ T^2
c_{Ge} (Å)	2.9589(6) - 6.5(2)$\times 10^{-6}$ T + 2.28(2)$\times 10^{-8}$ T^2
V_{Fe} (Å^3)	140.44(7) - 5,2(3)$\times 10^{-4}$ T + 3.12(3)$\times 10^{-6}$ T^2

	300 K	850 K
α_a (10^{-6} K^{-1})	3.34(9)	10.9(1)
$\alpha_{c_{Fe}}$ (10^{-6} K^{-1})	2.9(2)	9.7(2)
$\alpha_{c_{Ge}}$ (10^{-6} K^{-1})	2.5(1)	10.2(2)
β (10^{-6} K^{-1})	9.6(3)	31.5(5)

cause damages to the thermoelectric modules upon repeated thermal cycling.

4. Conclusion

The crystal structure of the Nowotny chimney-ladder $FeGe_\gamma$ with $\gamma \approx 1.52$ was studied from room temperature to its decomposition temperature at 850 K. An incommensurate composite crystal description of the structure with modulation wave vector $\boldsymbol{q}$ = (0, 0, 1.5191(1)) was used to fit the data, clearly indicating the incommensurate nature of the polycrystalline iron germanide. The γ value is significantly smaller in $FeGe_\gamma$ than in $MnSi_\gamma$. This is due to an elongation of the ladder [Ge] subsystem along the c axis caused by the larger atomic size of Ge. From room to high temperatures, the evolution of the lattice parameters a, c_{Fe} and c_{Ge} are described with a second order polynomial up to the peritectoid decomposition into FeGe and $FeGe_2$ at 850 K. The linear and volumetric thermal expansion parameters are multiplied by 4 and 3, respectively, from 300 to 850 K. Such thermal behavior is significantly different than $MnSi_\gamma$ and suggests that thermoelectric modules made of these materials would undergo high mechanical stress upon thermal cycling. However, the value of γ remains constant over the whole temperature range and would suggest a good stability of the

electronic transport properties in $FeGe_\gamma$ under operating conditions.

Acknowledgment

This work was supported by the Japan Society for the Promotion of Science (grants number PE19749 and 19H05819).

References

[1] T. Mori, Novel principles and nanostructuring methods for enhanced thermoelectrics, Small 13 (2017) 1702013. doi:10.1002/smll.201702013.

[2] T. Mori, S. Priya, Materials for energy harvesting: At the forefront of a new wave, MRS Bull. 43 (3) (2018) 176–180. doi:10.1557/mrs.2018.32.

[3] S. M. Pourkiaei, M. H. Ahmadi, M. Sadeghzadeh, S. Moosavi, F. Pourfayaz, L. Chen, M. A. P. Yazdi, R. Kumar, Thermoelectric cooler and thermoelectric generator devices: A review of present and potential applications, modeling and materials, Energy 186 (2019) 115849. doi:10.1016/j.energy.2019.07.179.

[4] I. Petsagkourakis, K. Tybrandt, X. Crispin, I. Ohkubo, N. Satoh, T. Mori, Thermoelectric materials and applications for energy harvesting power generation, Sci. Technol. Adv. Mat. 19 (1) (2018) 836–862. doi:10.1080/14686996.2018.1530938.

[5] D. Champier, Thermoelectric generators: A review of applications, Energy Convers. Manag 140 (2017) 167–181. doi:10.1002/aenm.201800056.

[6] W. Liu, Z. Chen, J. Zou, Eco-Friendly Higher Manganese Silicide Thermoelectric Materials: Progress and Future Challenges, Adv. Energy Mater. 8 (2018) 1800056. doi:10.1002/aenm.201800056.

[7] S. LeBlanc, S. K. Yee, M. L. Scullin, C. Dames, K. E. Goodson, Material and manufacturing cost considerations for thermoelectrics, Renew. Sust. Energ. Rev. 84 (2014) 313–317. doi:10.1016/j.rser.2013.12.030.

[8] Y. Miyazaki, D. Igarashi, K. Hayashi, T. Kajitani, K. Yubuta, Modulated crystal structure of chimney-ladder higher manganese silicides $MnSi_\gamma$ ($\gamma \approx 1.74$), Phys. Rev. B 78 (2008) 214104. doi:10.1103/PhysRevB.78.214104.

[9] Y. Miyazaki, Y. Kikuchi, Higher Manganese Silicide, $MnSi_\gamma$, Springer Berlin Heidelberg, 2013, pp. 141–156 (2013). doi:10.1007/978-3-642-37537-8_7.

[10] S. Le Tonquesse, V. Dorcet, L. Joanny, V. Demange, C. Prestipino, Q. Guo, D. Berthebaud, T. Mori, M. Pasturel, Mesostructure - thermoelectric properties relationships in $V_xMn_{1-x}Si_{1.74}$ (x = 0, 0.04) Higher Manganese Silicides prepared by magnesiothermy, J. Alloys Compd. 816 (2020) 152577. doi:10.1016/j.jallcom.2019.152577.

[11] G. Skomedal, L. Holmgren, H. M. andI.S. Eremin, G. Isachenko, M. Jaegle, K. Tarantik, N. Vlachos, M. Manoli, T. Kyratsi, D. Berthebaud, N. Y. D. Truong, F. Gascoin, Design, assembly and characterization of silicide-based thermoelectric modules, Energy Convers. Manag. 110 (2016) 13–21. doi:10.1016/j.enconman.2015.11.068.

[12] S. Le Tonquesse, Z. Verastegui, H. Huynh, V. Dorcet, Q. Guo, V. Demange, C. Prestipino, D. Berthebaud, T. Mori, M. Pasturel, Magnesioreduction Synthesis of Co-Doped β-$FeSi_2$: Mechanism, Microstructure, and Improved Thermoelectric Properties, ACS Appl. Energy Mater. 12 (2) (2019) 8525–8534. doi:10.1021/acsaem.9b01426.

[13] J. Bourgeois, J. Tobola, B. Wiendlocha, L. Chaput, P. Zwolenski, D. Berthebaud, F. Gascoin, Q. Recour, H. Scherrer, Study of Electron, Phonon and Crystal Stability Versus Thermoelectric Properties in Mg_2X(X = Si, Sn)

Compounds and Their Alloys, Funct. Mater. Lett. 6 (5) (2013) 1340005. doi:10.1142/S1793604713400055.

[14] K. Gerasimov, S. Pavlov, New equilibrium phase in the Fe-Ge system obtained by mechanical alloying, Intermetallics 8 (4) (2000) 451–452. doi:10.1016/S0966-9795(99)00113-2.

[15] W. Li, Y. Li, X. Ma, Z. Zhang, Incommensurate structure of a new Nowotny phase in Fe-Ge system, Mater. Chem. Phys. 148 (3) (2014) 490–493. doi:10.1016/j.matchemphys.2014.08.023.

[16] N. Sato, H. Ouchi, Y. Takagiwa, K. Kimura, Glass-like Lattice Thermal Conductivity and Thermoelectric Properties of Incommensurate Chimney-Ladder Compound $FeGe_{\gamma}$, Chem. Mater. 28 (2) (2016) 529–533. doi:10.1021/acs.chemmater.5b03952.

[17] V. Y. Verchenko, Z. Wei, A. A. Tsirlin, C. Callaert, A. Jesche, J. Hadermann, E. V. Dikarev, A. V. Shevelkov, Crystal Growth of the Nowotny Chimney-Ladder Phase Fe_2Ge_3 : Exploring New Fe-Based Narrow-Gap Semiconductor with Promising Thermoelectric Performance, Chem. Mater. 29 (23) (2017) 9954–9963. doi:10.1021/acs.chemmater.7b03300.

[18] V. Petříček, M. Dušek, L. Palatinus, Crystallographic Computing System JANA2006: General features, Z. Kristall. 229 (2014) 345–352. doi:10.1515/zkri-2014-1737.

[19] P. Thompson, D. E. Cox, J. B. Hastings, Rietveld refinement of Debye-Scherrer synchrotron X-ray data from Al_2O_3, J. Appl. Cryst. 20 (1987) 79–83. doi:10.1107/S0021889887087090.

[20] J.-F. Bérar, P. Lelann, E.s.d.'s and estimated probable error obtained in Rietveld refinements with local correlations, J. Appl. Cryst. 24 (1) (1991) 1–5. doi:10.1107/S0021889890008391.

[21] S. Van Smaalen, Incommensurate crystallography, Oxford University Press., 2007 (2007). doi:10.1093/acprof:oso/9780198570820.001.0001.

[22] S. Van Smaalen, Symmetry of composite crystals, Phys. Rev. B 43 (1991) 11330–11341. doi:10.1103/PhysRevB.43.11330.

[23] V. Petříček, K. Maly, P. Coppens, X. Bu, I. Cisarova, A. Frost-Jensen, The description and analysis of composite crystals, Acta Crystallogr. A 47 (1991) 210–216. doi:10.1107/S0108767390012065.

[24] A. Yamamoto, Determination of composite crystal structures and superspace groups, Acta Cryst. A 49 (6) (1993) 831–846. doi:10.1107/S0108767393004404.

[25] P. W. Stephens, Phenomenological model of anisotropic peak broadening in powder diffraction, J. Appl. Cryst. 32 (1999) 281–289. doi:10.1107/S0021889898006001.

[26] L. Akselrud, R. C. Gil, M. Wagner-Reetz, Y. Grin, Disorder in the composite crystal structure of the manganese 'disilicide' $MnSi_{1.73}$ from powder X-ray diffraction data, Acta Crystallogr. B 71 (2015) 707–712. doi:10.1107/S2052520615019757.

[27] H. G. Ye, S. Amelinckx, High-resolution electron microscopic study of manganese silicides $MnSi_{2-x}$, J. Solid State Chem. 61 (1986) 8–39. doi:10.1016/0022-4596(86)90003-4.

[28] S. Vivès, C. Navone, E. Gaudin, S. Gorsse, Improved microstructure and thermoelectric properties of higher manganese silicide processed by reactive spark plasma sintering, J. Mater. Sci. 52 (2017) 12826–12833. doi:10.1007/s10853-017-1397-7.

[29] Y. Kikuchi, T. Nakajo, K. Hayashi, Y. Miyazaki, High temperature X-ray diffraction study on incommensurate composite crystal $MnSi_{\gamma}$ (3+1)-

dimensional superspace approach, J. Alloys Compd. 616 (2014) 263–267. doi:10.1016/j.jallcom.2014.07.106.

[30] J. C. Slater, Atomic Radii in Crystals, J. Chem. Phys. 41 (1964) 3199. doi:10.1063/1.1725697.

[31] B. Lebeck, J. Bernhard, T. Freltoft, Magnetic structures of cubic FeGe studied by small-angle neutron scattering, J. Phys.: Condens. Matter. 1 (1989) 6105–6122. doi:10.1088/0953-8984/1/35/010.

[32] I. Piratinskaya, R. Krentsis, A. Mikhelson, P. Geld, Magnetic susceptibility of solid solutios $Fe_{x-1}Co_xGe_2$, Inorg. Mater. 4 (1975) 726–728.

[33] R. Andrusyak, B. Kotur, Phase equilibriums in the Sc-Mn-Ge and Sc-Fe-Ge systems at 870 K, Russ. Metall. 4 (1991) 204–208.

[34] P.-Y. Pichon, P. Berneron, J. Levinsky, A. Burema, G. Blake, D. Berthebaud, S. Gascoin, F. Gascoin, S. Hebert, J. Amtsfeld, T. Hommels, M. Huijben, J. de Boor, E. Müller, C. Navone, A. Schönecker, Stability and thermoelectric performance of doped higher manganese silicide materials solidified by RGS (ribbon growth on substrate) synthesis, J. Alloys Compd. (2020) 154602doi:https://doi.org/10.1016/j.jallcom.2020.154602.